Dynamic Threshold Adjustment-Based Event-Triggered Model Predictive Control for PMSM Motor

Junqiang Luo, Yixiao Luo, *Member, IEEE*, Kai Yang, *Senior Member, IEEE*, Md Sazzit Hossen, and Jincheng Yu, *Member, IEEE*

***Abstract*—This article proposes a dynamic threshold adjustment-based event-triggered (ET) strategy with finite control set model predictive control (FCS-MPC) for permanent magnet synchronous motor. A critical innovation is the dynamic adjustment of the threshold inequality in the ET technique. By incorporating the perturbation compensator to dynamically adjust the threshold, the event-triggering condition is unaffected by parameter drift and fast dynamic changes. In the absence of triggering, the control framework retains the control signal as constant. Upon fulfillment of the triggering condition, the FCS-MPC scheme is activated to generate an updated optimal control signal. To balance control performance and switching frequency, an adjustable coefficient is incorporated into the modified threshold inequality. The proposed method can flexibly reduce switching frequency while alleviating the computational burden by eliminating redundant operations. Extensive experimental studies validate the effectiveness of the proposed method.**

***Index Terms*—Dynamic threshold adjustment-based event-triggered (ET) strategy, finite control set model predictive control (FCS-MPC), permanent magnet synchronous motor (PMSM), switching frequency.**

I. Introduction

WITH the emergence of greater advanced microprocessors, finite control set model predictive control (FCS-MPC) has stood out for its simple implementation and flexibility in handling nonlinear constraints [1], [2]. These features enable FCS-MPC to achieve satisfactory control efficacy in permanent magnet synchronous motor (PMSM) drives, which is widely used in electric aircraft applications [3], [4].

Received 20 January 2025; revised 7 May 2025; accepted 7 June 2025. Date of publication 16 June 2025; date of current version 27 August 2025. This work was supported in part by the Natural Science Foundation of China under Grant 52307055 and in part by Delta Power Electronics Science and Education Development Plan under Grant DREG2024004. Recommended for publication by Associate Editor F D. Freijedo. *(Corresponding author: Yixiao Luo.)*

Junqiang Luo, Yixiao Luo, Kai Yang, and Md Sazzit Hossen are with the School of Electrical and Electronic Engineering, Huazhong University of Science and Technology, Wuhan 430074, China (e-mail: luojunqiang@hust.edu.cn; luoyx@hust.edu.cn; yk@hust.edu.cn; i202321053@hust.edu.cn).

Jincheng Yu is with the School of Mechanical Engineering and Automation, Harbin Institute of Technology Shenzhen, Shenzhen 518055, China (e-mail: yujincheng@hit.edu.cn).

Color versions of one or more figures in this article are available at https://doi.org/10.1109/TPEL.2025.3579870.

Digital Object Identifier 10.1109/TPEL.2025.3579870

However, in practical applications, FCS-MPC faces numerous limitations. One significant limitation is the occurrence of high switching loss due to high switching frequency [5]. The methods to reduce the switching frequency can generally be classified into four categories. The first one involves employing innovative pulse width modulation (PWM) techniques to reduce the switching frequency. In [6], diverse modulation techniques for reducing switching losses are summarized. It also clearly discusses the synchronous optimal PWM method, focusing on achieving low switching frequency. In [7], the synchronous optimal PWM method is employed to achieve low switching frequency operation for modular multilevel converter (MMC). Furthermore, a low-frequency carrier phase shifting modulation technique for MMC is proposed to decrease switching frequency during operation in [8]. However, these methods involve complex modulation strategies. The second category of methods is to use long-horizon prediction to reduce the switching frequency [9], [10]. Though long-horizon prediction offers superior performance compared to conventional prediction methods, its implementation is hindered by its significant computational resource requirements. The third approach involves incorporating a switching frequency constraint into the cost function [11], [12], [13]. In [13], two distinct cost functions are applied separately for steady-state and transient conditions, ensuring a low switching frequency in steady-state and a fast response during transients. Nevertheless, these methods are heavily reliant on weighting factors, and selecting appropriate weighting factors can be quite challenging. The last category is to reduce the switching frequency by optimizing the selection of control modes. In [14], the best voltage vector is selected based on optimization criteria using graph algorithms. This optimization not only ensures accurate current tracking but also reduces the switching frequency. To enhance spectral performance and reduce switching frequency, novel FCS-MPC schemes based on optimized pulse patterns are proposed in [15] and [16]. This method in FCS-MPC selects the optimal pattern from a predesigned pulse mode library for the next control step, based on the current state and predicted objectives. However, the drawbacks of this category include a complex control structure and high hardware requirements. Moreover, all the aforementioned methods aim to reduce switching frequency while neglecting the computational burden.

FCS-MPC typically determines the optimal control action by solving an online optimization problem in each control

cycle [17]. Nevertheless, this results in a substantial cumulative computational burden. In fact, the control actions generated by switch signals in many adjacent control cycles are almost identical. Therefore, it is worth considering removing the redundant switching signals from these control cycles to reduce the switching frequency and alleviate the computational burden [18]. Recent research has witnessed notable advancements in applying event-triggered (ET) techniques in MPC to reduce switching frequency [19]. ET control is a technique that dynamically determines system controller updates based on a triggering condition [20]. This control technique aims to reduce unnecessary control signal updates and thereby decrease the use of communication and computational resources [21]. In [22], a robust MPC method based on the dynamic ET mechanism was proposed for linear systems, and the triggering threshold was determined through interpolation strategies and optimization. However, this method is only applicable to linear systems, whereas motors are nonlinear and strongly coupled systems. In [23], an ET-MPC algorithm based on an ET mechanism and a dual-mode approach was proposed for unconstrained nonlinear systems. Nevertheless, the structure of this method is relatively complex, and its stability is affected by prediction errors. In [24], an integral-type ET condition designed based on the integral of the state estimation error was proposed. Unfortunately, integration processes may result in delayed responses to rapid disturbances or dynamic changes. An ET technique-based MPC for the power converter method is introduced in [25]. The method executes control actions only when the predesigned triggering condition is violated, showing significant advantages in reducing the switching frequency. Despite several ET-MPC schemes have been reported, none of them consider the impact of parameter drift or fast dynamic changes in motor drive systems on the threshold triggering condition, which may result in threshold variations. An increased threshold may excessively reduce triggering frequency, potentially compromising system control accuracy. Conversely, decreasing the threshold increases the switching frequency, leading to higher switching losses. Overall, it is essential to consider the impact of prediction errors within the ET control framework.

In view of the above-mentioned observations, this article presents a novel dynamic threshold adjustment-based ET-MPC scheme for PMSM with lower switching frequency. The proposed method utilizes an adjusted threshold inequality to activate control updates only when the control signal surpasses a predefined threshold. To facilitate this, a perturbation observer is introduced to dynamically adjust the threshold, ensuring that the triggering condition remains unaffected by parameter drift and fast dynamic changes. In the absence of triggering, the control signal is held constant. Through the elimination of redundant switching signals across consecutive control cycles, this method effectively reduces the switching frequency and alleviates the computational burden. In addition, to further balance control performance and switching frequency, an adjustable coefficient is introduced into the threshold inequality. Extensive experimental studies validate the effectiveness and feasibility of the proposed method.

The main contributions of this article are as follows.

1) A dynamic threshold adjustment mechanism is introduced into the ET-MPC framework, enabling real-time compensation for parameter drift and speed variations in the PMSM drive system. This ensures accurate triggering decisions under varying conditions, thereby enhancing control reliability.
2) Beyond switching frequency reduction, the alleviation of computational burden is considered an additional benefit of this method, since the complete MPC optimization is not required in many sampling periods in the proposed method.
3) The proposed control scheme incorporates an adjustable coefficient in the threshold inequality to allow users to fine-tune the balance between control performance and switching frequency based on specific application needs. This design provides the control scheme with broader applicability, making it suitable for complex conditions and diverse application scenarios.

II. Mathematical Model of PMSM

In the *d-q* frame, the dynamic behavior of the motor is simplified, allowing for more intuitive control. This article focuses on a surface-mounted PMSM (SPMSM) with equal *d-q* axis inductances. Therefore, the voltage equations of PMSM in the *d-q* frame are as follows:

$$\begin{cases} u_d = R_s i_d + L_s \frac{di_d}{dt} - \omega_e L_s i_q \\ u_q = R_s i_q + L_s \frac{di_q}{dt} + \omega_e (L_s i_d + \psi_f) \end{cases} \tag{1}$$

where R_s denotes the stator resistance; L_s denotes the stator inductances; i_d, i_q, u_d, u_q respectively denote the *d-q* axis currents and voltages; ψ_f denotes the permanent magnet flux linkage; ω_e denotes the electrical angular velocity, which can be assumed that is a constant in steady-state.

By selecting the *d-q* axis currents as state variables, (1) can be rewritten accordingly as

$$\dot{\boldsymbol{x}}_{dq}(t) = \boldsymbol{A}_{dq}\boldsymbol{x}_{dq}(t) + \boldsymbol{B}_{dq}\boldsymbol{u}_{dq}(t) + \boldsymbol{E}_{dq} \tag{2}$$

where $\boldsymbol{x}_{dq}(t) = [i_d\, i_q]^{\mathrm{T}}$, $\boldsymbol{u}_{dq}(t) = [u_d\, u_q]^{\mathrm{T}}$, $\boldsymbol{E}_{dq} = [0\ -\omega_e\psi_f/L_s]^{\mathrm{T}}$, $\boldsymbol{A}_{dq} = \begin{bmatrix} -\frac{R_s}{L_s} & \omega_e \\ -\omega_e & -\frac{R_s}{L_s} \end{bmatrix}$, $\boldsymbol{B}_{dq} = \begin{bmatrix} \frac{1}{L_s} & 0 \\ 0 & \frac{1}{L_s} \end{bmatrix}$.

III. Proposed Dynamic Threshold Adjustment-Based ET Method

To tackle the issue of high switching frequency, this article presents a dynamic threshold adjustment-based ET technology with FCS-MPC for PMSM. In this section, the details of the proposed strategy are presented.

A. ET-MPC Without Dynamic Adjustment

The control structure of the ET-MPC method is depicted in Fig. 1. The ET-MPC method updates control actions only when the predesigned triggering condition is violated, showing significant advantages in reducing the switching frequency.

To describe the ET-MPC process, we first define the time interval $[t_n, t_{n+1})$, where t_{n+1} is the triggering time when the

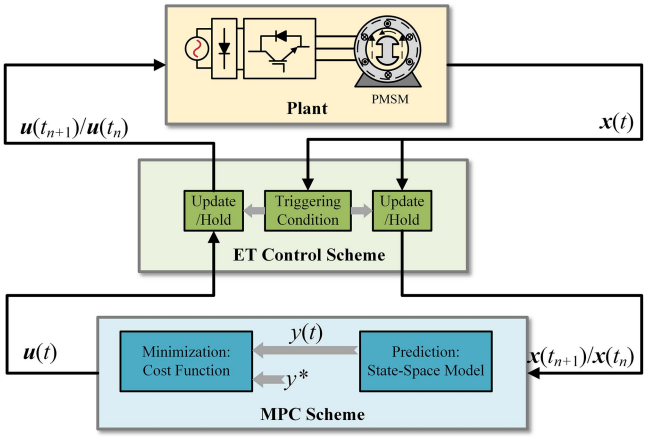

Fig. 1. Diagram of ET-MPC method.

activation triggering condition occurs. The relationship between t_n and t_{n+1} is as follows:

$$t_{n+1} = t_n + N \cdot T_s, N \in \mathbb{R}+ \tag{3}$$

where N denotes the number of cycles the event program operates until the preset condition is triggered; T_s represents the sampling period.

Remark 1: If there is no activation triggering condition within this time interval, the suggested control framework will not update after sending the control action $\boldsymbol{x}(t_n)$. When $t = t_{n+1}$, indicating that the activation triggering condition has been met, the suggested control framework will update the control action to $\boldsymbol{x}(t_{n+1})$.

Before determining the triggering condition, it is essential to define the error of the state variables through (2) as follows:

$$\boldsymbol{e}(t) = \boldsymbol{x}_{dq}(t_n) - \boldsymbol{x}_{dq}(t), t \in [t_n, t_{n+1}) \tag{4}$$

where $\boldsymbol{x}_{dq}(t_n)$ represents the state variables that have not been updated within the time interval $[t_n, t_{n+1})$.

To ensure input-to-state stability (ISS), it is necessary for $\boldsymbol{e}(t)$ to satisfy the following inequality:

$$\|\boldsymbol{e}(t)\| \leq \sigma\tau^{-1} \|\boldsymbol{x}_{dq}(t)\| \tag{5}$$

where σ and τ are κ_∞ class functions; σ and τ can be selected based on stability; $\|\cdot\|$ denotes the 2-norm.

The following derivations can be deduced according to (2) and (4):

$$\begin{aligned}
\frac{d\|\boldsymbol{e}(t)\|}{dt} &\leq \left\|\frac{d\boldsymbol{e}(t)}{dt}\right\| = \left\|\frac{d\boldsymbol{x}_{dq}(t)}{dt}\right\| \\
&= \|\boldsymbol{A}_{dq}\boldsymbol{x}_{dq}(t) + \boldsymbol{B}_{dq}\boldsymbol{u}_{dq}(t) + \boldsymbol{E}_{dq}\| \\
&\leq \|\boldsymbol{A}_{dq}\boldsymbol{x}_{dq}(t)\| + \|\boldsymbol{B}_{dq}\boldsymbol{u}_{dq}(t)\| + \|\boldsymbol{E}_{dq}\| \\
&\leq \|\boldsymbol{A}_{dq}\boldsymbol{e}(t)\| + \|\boldsymbol{A}_{dq}\boldsymbol{x}_{dq}(t_n)\| \\
&\quad + \|\boldsymbol{B}_{dq}\boldsymbol{u}_{dq}(t)\| + \|\boldsymbol{E}_{dq}\| \\
&\leq \|\boldsymbol{A}_{dq}\| \|\boldsymbol{e}(t)\| + \|\boldsymbol{A}_{dq}\boldsymbol{x}_{dq}(t_n)\| \\
&\quad + \|\boldsymbol{B}_{dq}\| u + \|\boldsymbol{E}_{dq}\|
\end{aligned} \tag{6}$$

where $\|\boldsymbol{u}_{dq}(t)\| \leq u$ in $[t_n, t_{n+1})$, $u \in \mathbb{R}_+$.

It can be seen that the upper bound inequality (6) is quite complex. For the sake of convenience in subsequent expressions, define

$$\Phi \triangleq \|\boldsymbol{e}(t)\| + \|\boldsymbol{A}_{dq}\|^{-1} \left(\|\boldsymbol{A}_{dq}\boldsymbol{x}_{dq}(t_n)\| + \|\boldsymbol{B}_{dq}\| u + \|\boldsymbol{E}_{dq}\|\right). \tag{7}$$

Therefore, (6) can be rewritten as

$$\dot{\Phi} \leq \|\boldsymbol{A}_{dq}\| \Phi \tag{8}$$

where $\dot{\Phi}$ is the derivative of Φ.

When $t = t_n$, according to the definition of Φ, we have

$$\Phi_{t_n} \triangleq \|\boldsymbol{A}_{dq}\|^{-1} \left(\|\boldsymbol{A}_{dq}\boldsymbol{x}_{dq}(t_n)\| + \|\boldsymbol{B}_{dq}\| u + \|\boldsymbol{E}_{dq}\|\right) \tag{9}$$

where $\boldsymbol{e}(t_n) = 0$ according to (4).

At this point, solving (8) yields the following inequality:

$$\begin{aligned}
\Phi &\leq \Phi_{t_n} e^{\left(\int_{t_n}^{t_{n+1}} \|\boldsymbol{A}_{dq}\| dx\right)} = \\
&\|\boldsymbol{A}_{dq}\|^{-1} \left(\|\boldsymbol{A}_{dq}\boldsymbol{x}_{dq}(t_n)\| + \|\boldsymbol{B}_{dq}\| u + \|\boldsymbol{E}_{dq}\|\right) \cdot e^{\|\boldsymbol{A}_{dq}\|(t-t_n)}.
\end{aligned} \tag{10}$$

Subsequently, substituting the definition of Φ into (10) gives the upper bound of $\|\boldsymbol{e}(t)\|$

$$\begin{aligned}
\|\boldsymbol{e}(t)\| \leq \|\boldsymbol{A}_{dq}\|^{-1} &\left(\|\boldsymbol{A}_{dq}\boldsymbol{x}_{dq}(t_n)\| + \|\boldsymbol{B}_{dq}\| u \right. \\
&\left. + \|\boldsymbol{E}_{dq}\|\right) \left(e^{\|\boldsymbol{A}_{dq}\|(t-t_n)} - 1\right).
\end{aligned} \tag{11}$$

The triggering condition for time t_{n+1} can be designed according to the upper bound of $\|\boldsymbol{e}(t)\|$

$$\begin{aligned}
\|\boldsymbol{e}(t_{n+1})\| > \|\boldsymbol{A}_{dq}\|^{-1} &\left(\|\boldsymbol{A}_{dq}\boldsymbol{x}_{dq}(t_n)\| + \|\boldsymbol{B}_{dq}\| u \right. \\
&\left. + \|\boldsymbol{E}_{dq}\|\right) \left(e^{\|\boldsymbol{A}_{dq}\|NT_s} - 1\right).
\end{aligned} \tag{12}$$

Hence, the threshold T for ET-MPC is set as

$$\begin{aligned}
T = \|\boldsymbol{A}_{dq}\|^{-1} &\left(\|\boldsymbol{A}_{dq}\boldsymbol{x}_{dq}(t_n)\| + \|\boldsymbol{B}_{dq}\| u \right. \\
&\left. + \|\boldsymbol{E}_{dq}\|\right) \left(e^{\|\boldsymbol{A}_{dq}\|NT_s} - 1\right)
\end{aligned} \tag{13}$$

where T is a positive number.

The threshold in ET-MPC techniques determines when the system updates the control input, which occurs when the state error exceeds the threshold. In motor control systems, ET-MPC is susceptible to prediction errors, which can lead to changes in the threshold.

B. Threshold Error Analysis

When considering prediction errors, the influence on the threshold formula originates from deviations in the system coefficient matrices $\boldsymbol{A}_{dq}$, $\boldsymbol{B}_{dq}$, and $\boldsymbol{E}_{dq}$. By substituting the matrix values from (2) into (13), the detailed threshold expression is derived as follows:

$$T = \left(\|\boldsymbol{x}_{dq}(t_n)\| + \frac{u + \omega_e\psi_f}{L_s\sqrt{\left(\frac{R_s}{L_s}\right)^2 + \omega_e^2}}\right)\left(e^{NT_s\sqrt{\left(\frac{R_s}{L_s}\right)^2+\omega_e^2}} - 1\right). \tag{14}$$

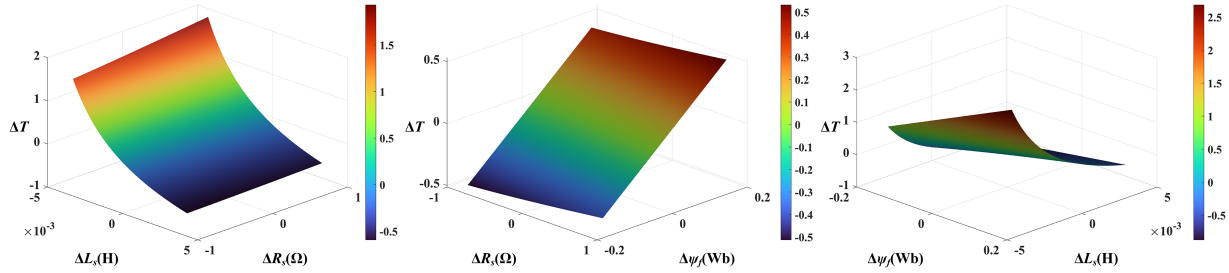

Fig. 2. Impact of parameter deviations on ΔT. (a) ΔL_s and ΔR_s impact on ΔT. (b) ΔR_s and $\Delta\psi_f$ impact on ΔT. (c) $\Delta\psi_f$ and ΔL_s impact on ΔT.

Further analysis reveals that variations in the resistance R_s, inductance L_s, flux linkage ψ_f and electrical angular velocity ω_e within the parameter matrix can introduce errors, thereby impacting the threshold formula. When the motor operates in steady state, variations in motor speed are not considered, the formula incorporating prediction errors is introduced as follows:

$$\begin{cases} R_{s0} = R_s + \Delta R_s \\ L_{s0} = L_s + \Delta L_s \\ \psi_{f0} = \psi_f + \Delta\psi_f \end{cases} \tag{15}$$

where R_s, L_s, and ψ_f represent the nominal values of resistance, inductance, and flux linkage, respectively; R_{s0}, L_{s0}, and ψ_{f0} represent the actual values of resistance, inductance, and flux linkage, respectively.

Incorporating these influences into the threshold formula yields a new threshold

$$T_{new} = \left(\|\boldsymbol{x}_{dq}(t_n)\| + \frac{u + \omega_e \psi_{f0}}{L_{s0}\sqrt{\left(\frac{R_{s0}}{L_{s0}}\right)^2 + \omega_e^2}} \right) \times \left(e^{NT_s\sqrt{\left(\frac{R_{s0}}{L_{s0}}\right)^2+\omega_e^2}} - 1 \right). \tag{16}$$

At this point, the difference in threshold variation can be obtained

$$\begin{aligned} \Delta T &= T_{\text{new}} - T \\ &= \|\boldsymbol{x}_{dq}(t_n)\| \left(e^{NTs\sqrt{\left(\frac{R_s+\Delta R_s}{L_s+\Delta L_s}\right)^2+\omega_e^2}} - e^{NTs\sqrt{\left(\frac{R_s}{L_s}\right)^2+\omega_e^2}} \right) \\ &+ \frac{u + \omega_e(\psi_f + \Delta\psi_f)}{L_s\sqrt{\left(\frac{R_s+\Delta R_s}{L_s+\Delta L_s}\right)^2 + \omega_e^2}} \left(e^{NTs\sqrt{\left(\frac{R_s+\Delta R_s}{L_s+\Delta L_s}\right)^2+\omega_e^2}} - 1 \right) \\ &- \frac{u + \omega_e\psi_f}{L_s\sqrt{\left(\frac{R_s}{L_s}\right)^2 + \omega_e^2}} \left(e^{NTs\sqrt{\left(\frac{R_s}{L_s}\right)^2+\omega_e^2}} - 1 \right). \end{aligned} \tag{17}$$

To assess the influence of parameter variations, a fixed operating condition is considered. The effect of parameter deviations on ΔT under rated operating conditions is depicted in Fig. 2. The parameter variation ranges from -0.5 to 0.5 times their nominal values. It can be observed that the threshold error ΔT is highly sensitive to variations in ΔL_s and $\Delta\psi_f$, where even slight parameter deviations can significantly increase ΔT. In contrast, the impact of ΔR_s on ΔT is relatively minor.

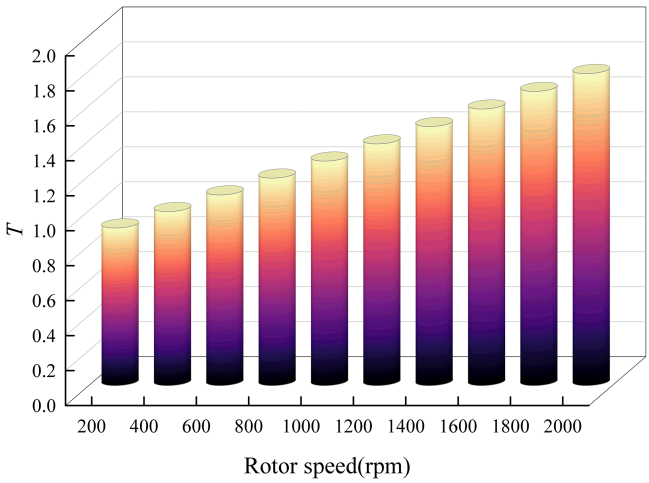

Fig. 3. Impact of rotor speed on threshold T.

To evaluate the influence of motor speed, the parameters are assumed to be accurate. Based on (14), the variation of the threshold with respect to speed is plotted in Fig. 3. It can be observed that the threshold increases approximately linearly with motor speed. Therefore, it can be concluded that rapid dynamics, such as changes in speed, may introduce non-negligible threshold errors.

Remark 2: All the above-mentioned analyses indicate that ET-MPC without threshold compensation is prone to triggering threshold distortion when facing parameter drift or fast dynamic conditions. Specifically, the threshold may become either too large or too small and fail to update in a timely manner. An excessively large threshold reduces the triggering frequency, which can significantly lower the switching frequency. However, this may come at the cost of reduced control accuracy. On the other hand, an overly small threshold maintains higher control sensitivity and accuracy but increases the switching frequency, leading to higher switching losses. Therefore, maintaining a properly regulated threshold is essential to balance control performance, efficiency, and hardware reliability in practical applications.

C. Proposed Dynamic Threshold Adjustment-Based ET Method

Based on the aforementioned analysis of the sources affecting the threshold, this article presents an innovative dynamic threshold adjustment-based ET-MPC method for PMSM. The

proposed method employs a perturbation compensator to dynamically adjust the threshold.

First, errors caused by variations in the system parameters are considered comprehensively. Thus, (2) is rewritten as a new state-space equation

$$\dot{\boldsymbol{x}}_{dq}(t) = \boldsymbol{A}_{dq}\boldsymbol{x}_{dq}(t) + \boldsymbol{B}_{dq}\boldsymbol{u}_{dq}(t) + \boldsymbol{E}_{dq} + \boldsymbol{f}_{dq}(t) \tag{18}$$

where $\boldsymbol{f}_{dq}(t) = [f_d(t)\, f_q(t)]^{\mathrm{T}}$. $f_d(t)$ and $f_q(t)$ respectively represent the total errors on the *d*-*q* axis.

With the compensator applied, (18) is rewritten as

$$\begin{cases} \boldsymbol{e}_{\text{rror}} = \boldsymbol{z}_{1dq}(t) - \boldsymbol{x}_{dq}(t) \\ \dot{\boldsymbol{z}}_{1dq}(t) = \boldsymbol{A}_{dq}\boldsymbol{x}_{dq}(t) + \boldsymbol{B}_{dq}\boldsymbol{u}_{dq}(t) + \boldsymbol{E}_{dq} + \boldsymbol{z}_{2dq}(t) - c_1\boldsymbol{e}_{\text{rror}} \\ \dot{\boldsymbol{z}}_{2dq}(t) = -c_2\boldsymbol{e}_{\text{rror}} \end{cases} \tag{19}$$

where $\boldsymbol{z}_{1\,dq}(t)$ represents the estimated *d*-*q* axis currents; $\boldsymbol{z}_{2\,dq}(t)$ represents the total errors $\boldsymbol{f}_{dq}(t)$; c_1 and c_2 are the gains of the compensator, $c_1 = 2\omega_c^2$, $c_2 = \omega_c$, $\omega_c$is the ideal bandwidth of the compensator.

The error of the state errors (4) is rewritten as

$$\hat{\mathbf{e}}(t) = \boldsymbol{z}_{1dq}(t_n) - \boldsymbol{z}_{1dq}(t), t \in [t_n, t_{n+1}) \tag{20}$$

where $\boldsymbol{z}_{1\,dq}(t_n)$ represents the estimated state variables that have not been updated within the time interval $[t_n,\ t_{n+1})$.

According to (20), the conclusions below can be inferred

$$\begin{aligned} \frac{d\,\|\hat{\mathbf{e}}(t)\|}{dt} &\le \left\|\frac{d\hat{\mathbf{e}}(t)}{dt}\right\| = \left\|\frac{d\boldsymbol{z}_{1dq}(t)}{dt}\right\| \\ &= \|\boldsymbol{A}_{dq}\boldsymbol{x}_{dq}(t) + \boldsymbol{B}_{dq}\boldsymbol{u}_{dq}(t) + \boldsymbol{E}_{dq} + \boldsymbol{z}_{2dq}(t) - c_1\boldsymbol{e}_{\text{rror}}\| \\ &= \|\boldsymbol{A}_{dq}\boldsymbol{x}_{dq}(t) + \boldsymbol{B}_{dq}\boldsymbol{u}_{dq}(t) + \boldsymbol{E}_{dq} + \boldsymbol{z}_{2dq}(t) \\ &\quad + c_1\boldsymbol{x}_{dq}(t) + c_1\hat{\mathbf{e}}(t) - c_1\boldsymbol{z}_{1dq}(t_n)\| \\ &\le c_1\|\boldsymbol{x}_{dq}(t)\| + c_1\|\hat{\mathbf{e}}(t)\| + c_1\|\boldsymbol{z}_{1dq}(t_n)\| + \|\boldsymbol{A}_{dq}\boldsymbol{x}_{dq}(t)\| \\ &\quad + \|\boldsymbol{B}_{dq}\boldsymbol{u}_{dq}(t)\| + \|\boldsymbol{E}_{dq}\| + \|\boldsymbol{z}_{2dq}(t)\| \end{aligned} \tag{21}$$

where $\|\boldsymbol{x}_{dq}(t)\| \le x$ in the time interval $[t_n, t_{n+1})$, $\|\boldsymbol{z}_{2\,dq}(t)\| \le z$ in the time interval $[t_n, t_{n+1})$, $x \in \mathbb{R}_+$and $z \in \mathbb{R}_+$.

By redefining Φ, we obtain

$$\begin{aligned} \Phi \triangleq\ & \|\hat{\mathbf{e}}(t)\| + \left(x + \|\boldsymbol{z}_{1dq}(t_n)\| + \frac{1}{c_1}\|\boldsymbol{A}_{dq}\|\,x\right. \\ & \left. + \frac{1}{c_1}\|\boldsymbol{B}_{dq}\|\,u + \frac{1}{c_1}\|\boldsymbol{E}_{dq}\| + \frac{1}{c_1}z\right). \end{aligned} \tag{22}$$

Therefore, (21) can be rewritten as

$$\dot{\Phi} \le c_1\Phi \tag{23}$$

where $\dot{\Phi}$ is the derivative of Φ.

Subsequently, the solution of (23) is given by

$$\begin{aligned} \Phi &\le \Phi_{t_n} e^{\left(\int_{t_n}^{t_{n+1}} c_1 dx\right)} \\ &= \left(x + \|\boldsymbol{z}_{1dq}(t_n)\| + \frac{1}{c_1}\|\boldsymbol{A}_{dq}\|\,x + \frac{1}{c_1}\|\boldsymbol{B}_{dq}\|\,u\right. \\ &\quad \left. + \frac{1}{c_1}\|\boldsymbol{E}_{dq}\| + \frac{1}{c_1}z\right) \cdot e^{c_1(t_{n+1}-t_n)} \end{aligned} \tag{24}$$

where $\hat{\mathbf{e}}(t_n) = 0$.

Next, substituting the definition of Φ into (24) results in

$$\begin{aligned} \|\hat{\mathbf{e}}(t)\| \le\ & \left(x + \|\boldsymbol{z}_{1dq}(t_n)\| + \frac{1}{c_1}\|\boldsymbol{A}_{dq}\|\,x + \frac{1}{c_1}\|\boldsymbol{B}_{dq}\|\,u\right. \\ & \left. + \frac{1}{c_1}\|\boldsymbol{E}_{dq}\| + \frac{1}{c_1}z\right) \cdot \left(e^{c_1(t_{n+1}-t_n)} - 1\right). \end{aligned} \tag{25}$$

Then, the upper bound inequality of $\|\hat{\mathbf{e}}(t_{n+1})\|$ is employed to inform the formulation of the triggering condition. Therefore, based on the inequality satisfying the ISS condition, a suitable triggering mechanism can be established as

$$\begin{aligned} \|\hat{\mathbf{e}}(t_{n+1})\| > \zeta & \left(x + \|\boldsymbol{z}_{1dq}(t_n)\| + \frac{1}{c_1}\|\boldsymbol{A}_{dq}\|\,x + \frac{1}{c_1}\|\boldsymbol{B}_{dq}\|\,u\right. \\ & \left. + \frac{1}{c_1}\|\boldsymbol{E}_{dq}\| + \frac{1}{c_1}z\right) \cdot \left(e^{c_1 NT_s} - 1\right) \end{aligned} \tag{26}$$

where $\zeta \in (0,1]$ is adjustable to balance the tuning performance and switching frequency. This ensures that FCS-MPC can flexibly reduce the switching frequency.

Before applying the triggering conditions to FCS-MPC, discretization processing is required. The estimation of the state variable error needs to be rewritten as

$$\hat{\mathbf{e}}(l) = \boldsymbol{z}_{1dq}(n) - \boldsymbol{z}_{1dq}(l), l \in [n, n+N). \tag{27}$$

The threshold triggering condition after discretization is as follows:

$$\begin{aligned} \|\hat{\mathbf{e}}(n+N)\| > \zeta & \left(x + \|\boldsymbol{z}_{1dq}(n)\| + \frac{1}{c_1}\|\boldsymbol{A}_{dq}\|\,x + \frac{1}{c_1}\|\boldsymbol{B}_{dq}\|\,u\right. \\ & \left. + \frac{1}{c_1}\|\boldsymbol{E}_{dq}\| + \frac{1}{c_1}z\right) \cdot \left(e^{c_1 NT_s} - 1\right). \end{aligned} \tag{28}$$

The proposed dynamic threshold adjustment-based ET technique workflow is displayed in Fig. 4. Although *n* and *N* vary, their sum always equals *k* + 1. The diagram of the predicted current trajectory is depicted in Fig. 5. When the triggering condition is not met, the technique maintains the control signal unchanged, effectively reducing the number of switching events. Upon fulfillment of the triggering condition, the MPC scheme activates and updates control actions. As can be observed, the MPC scheme is activated to update the control signal only when the threshold inequality (28) is satisfied.

The state variables at time *n* or time *n* + *N* can be provided to the FCS-MPC based on whether the threshold triggering condition is met. The specific situation is as follows:

$$\boldsymbol{i}_{dq}(k+1) = \begin{cases} \boldsymbol{z}_{1dq}(n), & \text{when (28) is not met} \\ \boldsymbol{z}_{1dq}(n+N), & \text{when (28) is met} \end{cases}. \tag{29}$$

Considering one-step delay compensation, the current equation is rewritten as follows:

$$\begin{aligned} \boldsymbol{i}_{\boldsymbol{dq}}(k+2) = & T_s(\boldsymbol{I} + \boldsymbol{A}_{dq})\boldsymbol{i}_{dq}(k+1) + T_s\boldsymbol{z}_{2dq}(k+1) \\ & + T_s\boldsymbol{B}_{dq}\boldsymbol{u}_{dq}(k+1) + T_s\boldsymbol{E}_{dq} \end{aligned} \tag{30}$$

where $\boldsymbol{i}_{\boldsymbol{dq}}(k+2)$ indicates the *d*-*q* axis currents after delay compensation.

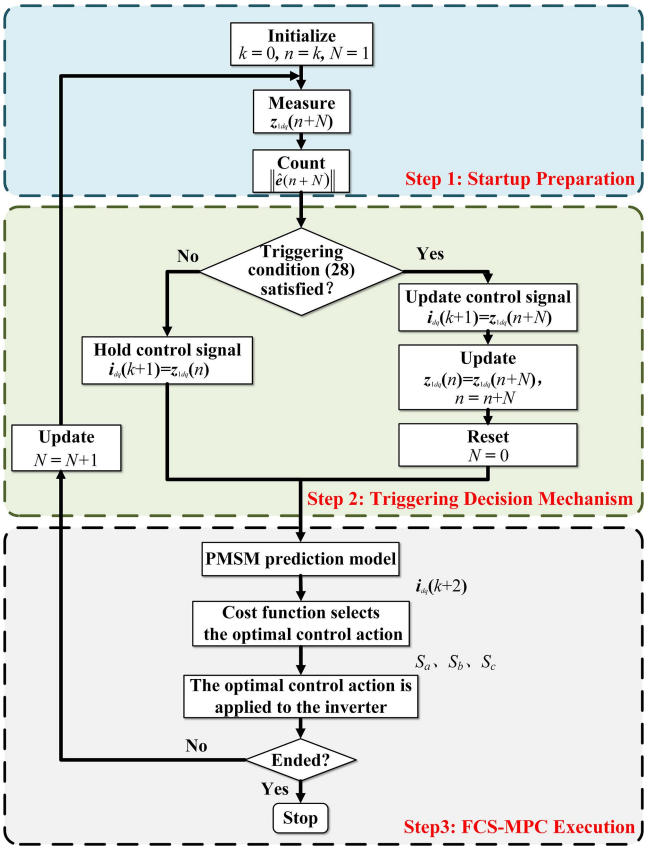

Fig. 4. Workflow of proposed method.

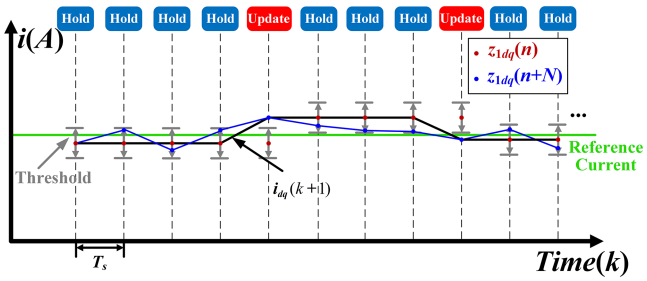

Fig. 5. Predicted current trajectory of the proposed method.

By minimizing the cost function, the controller can select the optimal control actions to achieve the desired objectives. The cost function selected after delay compensation is as follows:

$$g_{\text{opt}} = \left|i_d^{\text{ref}} - i_d(k+2)\right| + \left|i_q^{\text{ref}} - i_q(k+2)\right| \tag{31}$$

where i_d^{ref} and i_q^{ref} indicate the d-q axis reference currents.

Remark 3: The proposed method introduces both a threshold inequality and a dynamic threshold compensation mechanism into the FCS-MPC framework. While these additions introduce slight structural complexity, they do not alter the fundamental design of the original FCS-MPC. The threshold inequality serves as a decision layer for triggering control updates, and the dynamic compensation mechanism enhances adaptability under system variations. Both components are modular, allowing for seamless integration into existing FCS-MPC implementations without significantly increasing design or implementation complexity.

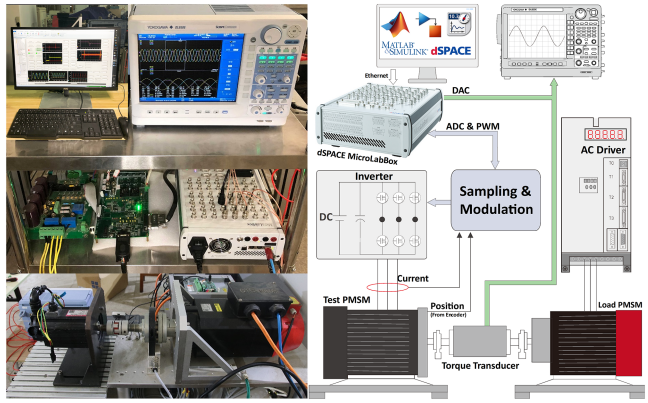

Fig. 6. Experimental platform.

TABLE I
PARAMETERS OF MACHINE

Specification	Value
Rated power P	1.25 kW
Rated torque T_e	6 N·m
Rated speed n	2000 rpm
Number of pole pairs P_n	2
Stator resistance R_s	1.8 Ω
d-q axis stator inductance L	7.6 mH
Flux linkage ψ_f	0.33 Wb

Remark 4: Regarding computational complexity, the control actions produced by switching signals in many adjacent control cycles are almost identical. The proposed mechanism eliminates redundant switching signals, thereby reducing the number of optimization problems to be solved in FCS-MPC. The additional computational task only involves evaluating threshold inequalities, which is a simple comparison operation. Compared to the overall computational load of FCS-MPC, this additional computation is negligible. Therefore, the computational burden of the entire system is reduced.

IV. EXPERIMENTAL RESULTS

To confirm the efficacy of the proposed approach, experiments are conducted on a 1.25-kW SPMSM in this article. The experimental platform is illustrated in Fig. 6. The parameters of the SPMSM are presented in Table I. The experimental setup utilizes a dSPACE MicroLabBox for real-time control implementation. A three-phase voltage source inverter is built using the Infineon insulated-gate bipolar transistor module FF300R12ME4. To comprehensively demonstrate the superiority of the proposed strategy, experiments are carried out for three scenarios: traditional FCS-MPC (Algorithm 1), ET-MPC without dynamic adjustment (Algorithm 2) and the proposed dynamic threshold adjustment-based ET-MPC (Algorithm 3). The performance of the three algorithms is comparatively assessed under conditions of similar switching frequency and identical sampling frequency. In addition, the switching frequency analysis and computational burden analysis of each control scheme are analyzed to further

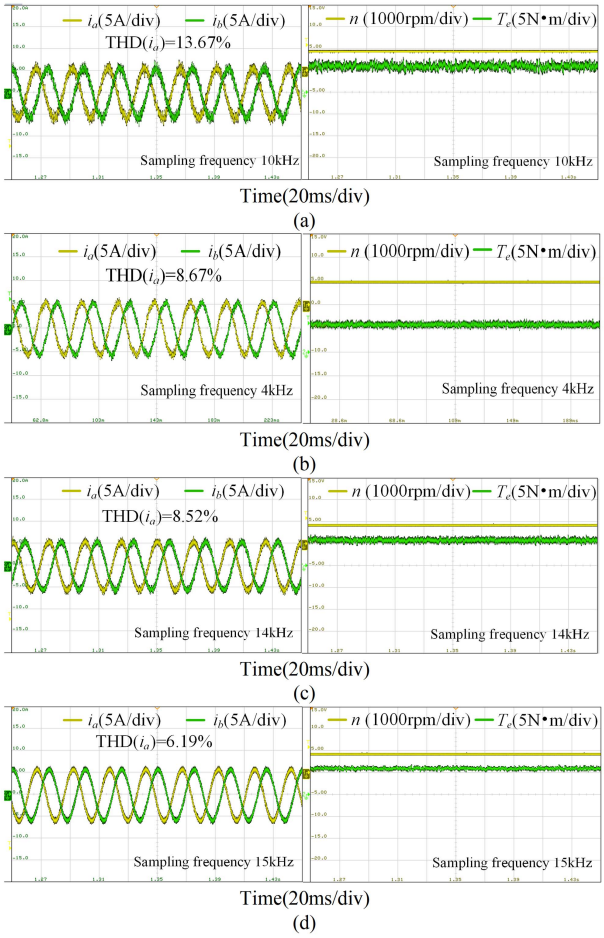

Fig. 7. Steady state performance with rated load at 1000 r/min under similar switching frequency of 3975 Hz. (a) Algorithm 1. (b) DPCC method. (c) Algorithm 2. (d) Algorithm 3 ($\zeta = 0.5$).

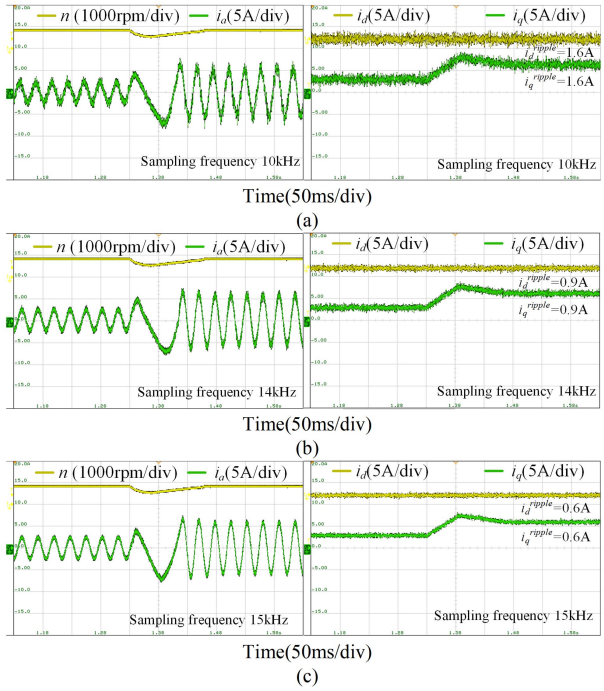

Fig. 8. Step load change performance from 0 to 6 N·m under similar switching frequency of 3975 Hz. (a) Algorithm 1. (b) Algorithm 2. (c) Algorithm 3 ($\zeta = 0.5$).

demonstrate the practical benefits of the proposed dynamic threshold compensation strategy.

A. *Similar Switching Frequency Experimental Results*

To explore the differences in current quality and control performance when targeting a specific switching frequency, comparative experiments were conducted under the scenario of "similar switching frequency with different sampling rates" for the three algorithms.

1) Steady State Performance Comparison: First, the steady-state performance comparisons of the three algorithms and single-sampling single-update deadbeat predictive current control (DPCC) under a similar switching frequency of 3975 Hz are depicted in Fig. 7. As shown in Fig. 7(a)–(d), the sampling frequencies are set to 10, 4, 14, and 15 kHz, respectively, resulting in switching-to-sampling frequency ratios of approximately 39.75%, 100%, 28.39%, and 26.50% . Notably, the proposed Algorithm 3 achieves the lowest switching-to-sampling frequency ratio among the four. Compared to conventional FCS-MPC and DPCC, the proposed ET-MPC method demonstrates lower current distortion, reducing the total harmonic distortion (THD) from 13.67% to 6.19% . This is because, under the identical switching loss constraint, the proposed ET strategy allows the use of a higher sampling frequency, which improves current tracking and reduces ripple. Higher sampling frequency shortens the update interval for current, voltage, and speed measurements. This allows the current deviation from its reference value between two consecutive predictions to be smaller, which reduces error accumulation and consequently leads to lower current ripple. In addition, the dynamic adjustment mechanism further mitigates the impact of prediction errors on threshold triggering, enhancing control performance.

2) Step Load Variation Performance Comparison: The comparative experiments on step load variation performance are illustrated in Fig. 8. As can be observed, the load suddenly steps from 0 to 6 N·m when the motor is running at 1000 r/min. On the one hand, the transient period of speed change in all three scenarios is approximately 130 ms. The motor speed decreases as the load increases and then promptly returns to the set speed. A rise in load leads to a corresponding increase in phase current magnitude. The dynamic response performance of the three scenarios is comparable. At the same time, the current quality of all scenarios aligns with the results discussed above. Under similar switching frequency, the conventional FCS-MPC method exhibits a q-axis current ripple of 1.6 A at steady state, whereas the proposed Algorithm 3 achieves a q-axis current ripple of 0.6 A.

3) Acceleration Variation Performance Comparison: A comparative evaluation of acceleration performance from standstill to 800 r/min is illustrated in Fig. 9. Under similar switching frequency, the speed waveforms during acceleration for all methods exhibit smoothness. A settling time of approximately

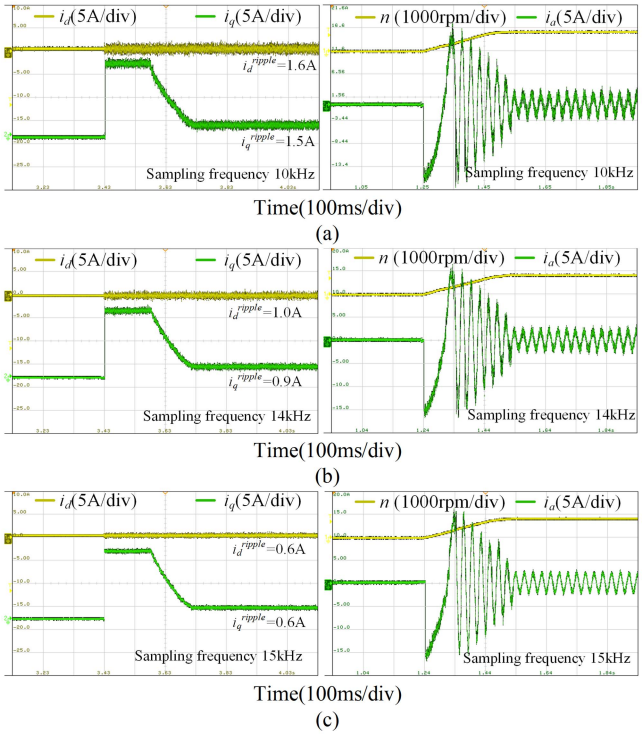

Fig. 9. Acceleration performance from 0 to 800 r/min under similar switching frequency of 3975 Hz. (a) Algorithm 1. (b) Algorithm 2. (c) Algorithm 3 ($\zeta = 0.5$).

300 ms is observed to reach steady-state conditions. During the transient period, both the phase currents and *d-q* axis currents exhibit smoothness. The ET methods exhibit significantly superior current quality compared to conventional FCS-MPC upon reaching steady-state conditions. In addition, the proposed method displays better current quality compared to the ET-MPC without dynamic adjustment. The magnitude of the *d-q* current ripple is in accordance with the preceding analysis.

B. Identical Sampling Frequency Experimental Results

To more intuitively quantify the actual contribution of the proposed method to switching frequency reduction, performance comparison experiments for the three algorithms were conducted under the identical sampling frequency of 15 kHz.

1) Steady State Performance Comparison: The steady-state performance of three algorithms is evaluated under rated load at the speed of 1000 r/min, as shown in Fig. 10. To highlight the differences in current harmonic distribution among the three algorithms, the fast Fourier transform (FFT) analysis of phase current i_a is evaluated in Fig. 11. As observed from Fig. 10 and 11, Algorithm 1 achieves the lowest total THD of 5.12%, owing to the full execution of MPC optimization in each control cycle. In comparison, Algorithm 2 exhibits a higher THD of 7.41%, which results from the reduced switching frequency introduced by the ET mechanism. The proposed Algorithm 3 with $\zeta = 0.5$ demonstrates a favorable tradeoff, achieving a THD of 6.19% while reducing the frequency of control updates. These results confirm the effectiveness of the proposed ET mecha-

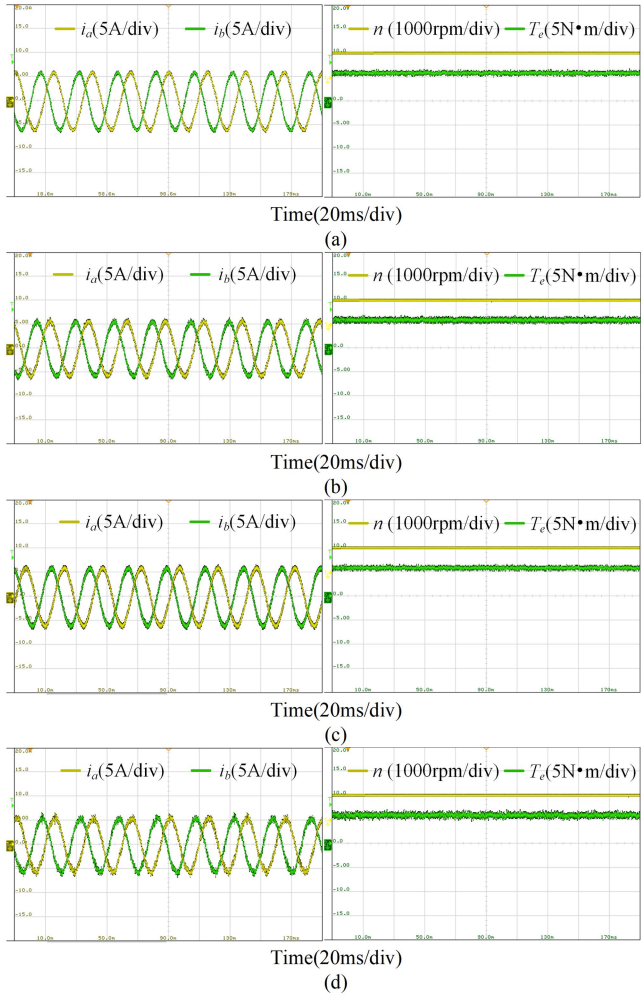

Fig. 10. Steady-state performance with rated load at 1000 r/min under the identical sampling frequency 15 kHz. (a) Algorithm 1. (b) Algorithm 2. (c) Algorithm 3 ($\zeta = 0.5$). (d) Algorithm 3 ($\zeta = 0.9$).

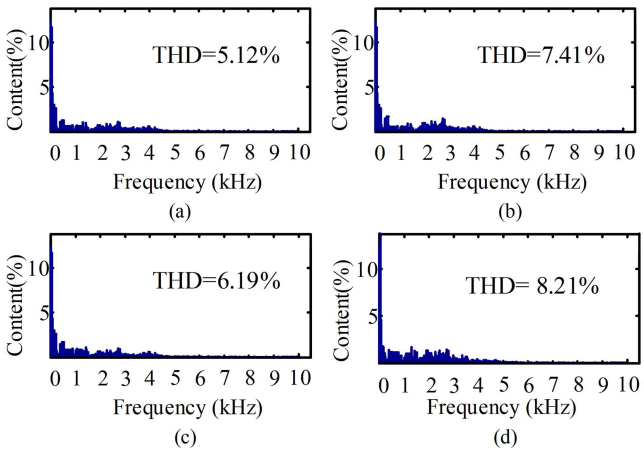

Fig. 11. FFT analysis of phase current i_a for all three algorithms under the identical sampling frequency 15 kHz. (a) Algorithm 1. (b) Algorithm 2. (c) Algorithm 3 ($\zeta = 0.5$). (d) Algorithm 3 ($\zeta = 0.9$).

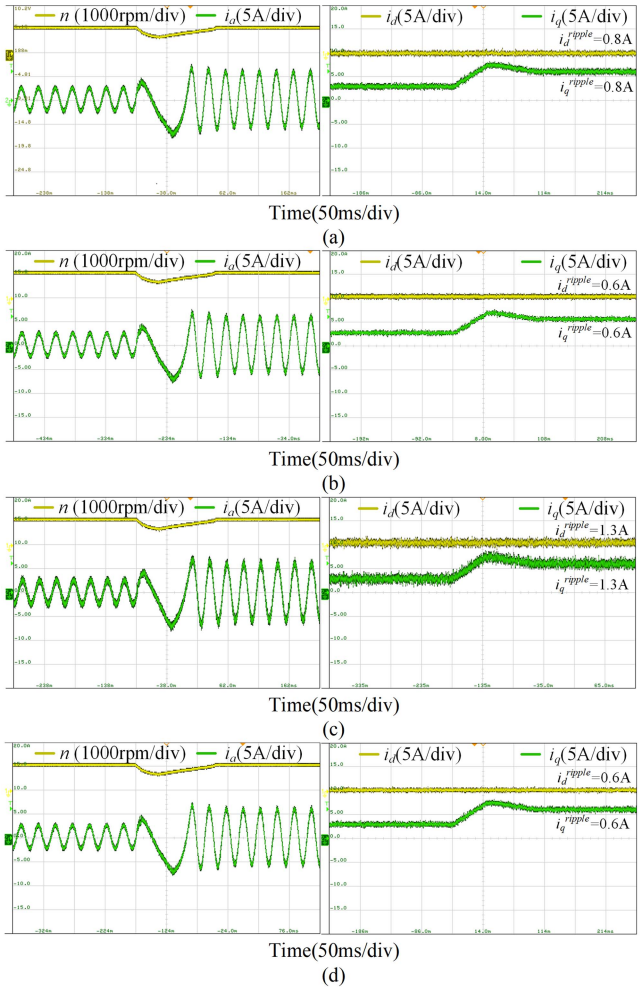

Fig. 12. Step load change performance from 0 to 6 N·m under the speed of 1000 r/min with accurate parameters at the identical sampling frequency 15 kHz. (a) Algorithm 2 with accurate parameters. (b) Algorithm 3 ($\zeta = 0.5$) with accurate parameters. (c) Algorithm 2 with mismatched parameters (150% R_s, 150% L_s, and 50% ψ_f). (d) Algorithm 3 ($\zeta = 0.5$) with mismatched parameters (150% R_s, 150% L_s, and 50% ψ_f).

nism in significantly reducing the switching frequency without substantially compromising current control performance. Moreover, increasing the adjustable coefficient from 0.5 to 0.9 leads to a controlled increase in THD to 8.21%, attributed to a higher triggering threshold and reduced update frequency. This behavior highlights the flexibility of the proposed approach, where the coefficient ζ can be tuned according to application-specific demands to balance switching frequency and current quality.

2) Transient State Performance Comparison: To more clearly verify the advantages of the proposed method in terms of robustness and dynamic response, a step-load change comparison experiment between Algorithm 2 and Algorithm 3 was conducted under the identical sampling frequency of 15 kHz, as shown in Fig. 12. Since Algorithm 1 performs full prediction and optimization at every sampling instant without incorporating an ET mechanism, comparing Algorithm 2 and Algorithm 3 within the same ET control framework is more suitable for isolating the impact of the proposed dynamic threshold compensation mechanism.

TABLE II
IMPACT OF THE ADJUSTABLE COEFFICIENT ON SWITCHING FREQUENCY AND CONTROL PERFORMANCE WITH RATED SPEED 2000 R/MIN UNDER IDENTICAL SAMPLING FREQUENCY 15 KHZ

adjustable coefficient ζ	0.2	0.4	0.6	0.8	1
switching frequency (Hz)	4330	4120	3785	3420	3265
current THD (%)	5.3	5.8	6.5	7.1	8.4

As observed from Fig. 12(a) and (b) under accurate parameter conditions, both two algorithms exhibit a noticeable speed drop after the load change, followed by a gradual recovery to steady-state, with overall dynamic response performance being roughly comparable. In terms of current quality, Algorithm 2 produces a ripple amplitude of approximately 0.8 A, whereas Algorithm 3 ($\zeta = 0.5$) maintains a smaller ripple of around 0.6 A. Under parameter mismatch conditions (150% R_s, 150% L_s, and 50% ψ_f), as illustrated in Fig. 12(c) and (d), Algorithm 2 exhibits significantly degraded performance. The current ripple increases sharply to 1.3 A, and the waveform becomes notably distorted, highlighting its sensitivity to parameter uncertainties. Conversely, Algorithm 3 maintains relatively stable behavior with a ripple amplitude still around 0.6 A and no evident degradation in speed recovery or current response. These results effectively confirm that the dynamic threshold compensation mechanism can suppress trigger failures and performance degradation caused by prediction errors under parameter mismatch, significantly improving the current quality and the stability of the ET-MPC mechanism.

3) Field-Weakening Region Performance Comparison: To further validate the adaptability of the proposed strategy, a comparative experimental study was conducted under both rated speed and field-weakening conditions. Specifically, the motor was operated at the rated speed of 2000 r/min and at 2400 r/min (120% of the rated speed) by employing a leading-angle flux-weakening strategy [26], while maintaining the identical sampling frequency of 15 kHz for all three algorithms. The comparative results under the rated-speed condition are presented in Fig. 13, and those under the field-weakening condition are shown in Fig. 14. In addition, the impact of the adjustable coefficient ζ on switching frequency and system control performance with rated speed 2000 r/min is illustrated in Table II.

As shown in Fig. 13, Algorithm 1 achieves the lowest THD of 5.14% and best current quality at the rated speed of 2000 r/min. However, this comes with a higher number of switching actions. In contrast, Algorithm 2 reduces the switching frequency using the ET mechanism, but increases the current THD to 7.59% . Algorithm 3 with $\zeta = 0.5$ slightly improves current THD to 6.19% over Algorithm 2, while maintaining a switching frequency lower than Algorithm 1. A longitudinal comparison shows that for Algorithm 2, current THD increases from 7.41% to 7.59% as the speed rises from 1000 to 2000 r/min. This is mainly due to the lack of threshold compensation in ET-MPC, making it more sensitive to speed variations, consistent with the earlier theoretical analysis. Unlike Algorithm 2, Algorithm 3

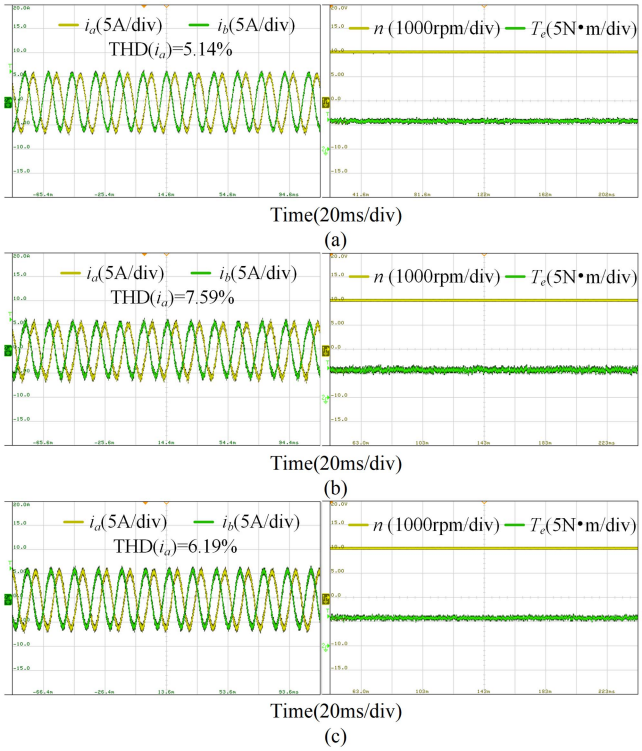

Fig. 13. Steady-state performance with rated load at rated speed 2000 r/min under the identical sampling frequency 15 kHz. (a) Algorithm 1. (b) Algorithm 2. (c) Algorithm 3 ($\zeta = 0.5$).

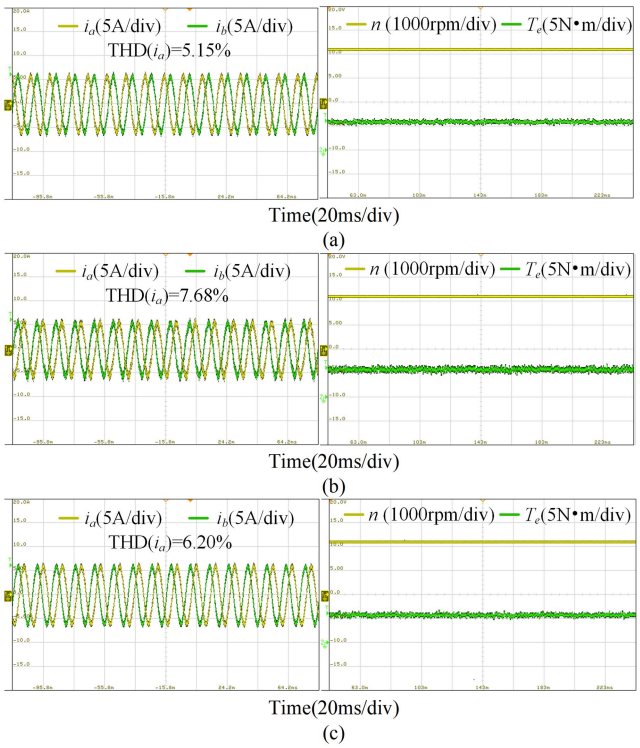

Fig. 14. Steady-state performance with rated load at 120% of the rated speed 2400 r/min under the identical sampling frequency 15 kHz. (a) Algorithm 1. (b) Algorithm 2. (c) Algorithm 3 ($\zeta = 0.5$).

maintains nearly consistent current quality across different speeds, demonstrating better stability. This further confirms that the proposed Algorithm 3 effectively mitigates threshold errors caused by speed variations, enhancing the stability of the triggering condition and improving system robustness.

As observed from Table II, as the adjustable coefficient in the threshold inequality increases, the interval for updating the control signals in the MPC scheme also lengthens. The switching frequency of the control signal exhibits a decreasing trend as the coefficient increases. As the coefficient increases from 0.2 to 1 under the identical sampling frequency 15 kHz, the THD increases from 5.3% to 8.4% . Adjusting this coefficient helps in fine-tuning the balance between control precision and switching frequency. The switching frequency exhibits a downward trend from 4330 to 3265 Hz as the coefficient is increased from 0.2 to 1. Therefore, the adjustable coefficient ζ can flexibly balance control performance and switching frequency, thereby significantly increasing the flexibility of the control system.

Fig. 14 presents the control results at an elevated speed of 2400 r/min. As shown in Fig. 14, the overall trends in current quality remain consistent with those observed at the rated speed. Algorithm 2 exhibits a further decline in current quality under field-weakening conditions, mainly due to the increased threshold error at higher speeds, which intensifies deviations in the triggering condition and reduces the number of effective triggering events. In contrast, Algorithm 3 continues to maintain stable switching frequency and current quality in this high-speed region, demonstrating superior stability under field-weakening operation.

C. Switching Frequency Analysis

The effectiveness of the proposed method in reducing the switching frequency is evaluated in this subsection under the identical sampling frequency of 10 kHz. By counting the number of switching transitions in the upper arms of the three-phase inverter over k sampling cycles for each of the three phases, the switching frequency for each phase can be calculated as follows:

$$f_x = \frac{\sum_{i=1}^{k} \left| S_x^i - S_x^{i-1} \right|}{2kT_s}, x = a, b, c \tag{32}$$

where the denominator term "2" accounts for both rising and falling edges in a single switching action.

Thus, the average switching frequency (ASF) is

$$f_{\text{ASF}} = \frac{f_a + f_b + f_c}{3}. \tag{33}$$

Fig. 15 compares the ASF for all three algorithms at the identical sampling frequency of 10 kHz. The conventional Algorithm 1 exhibits the highest switching frequency across the entire speed range. Conversely, Algorithms 2 and 3 significantly reduce the ASF by introducing the ET mechanism. However, the ASF of Algorithm 2, which adopts a static threshold, decreases noticeably as speed increases. This is because the threshold increases with speed, leading to a lower triggering frequency, which is consistent with the threshold error analysis in Fig. 3. On the

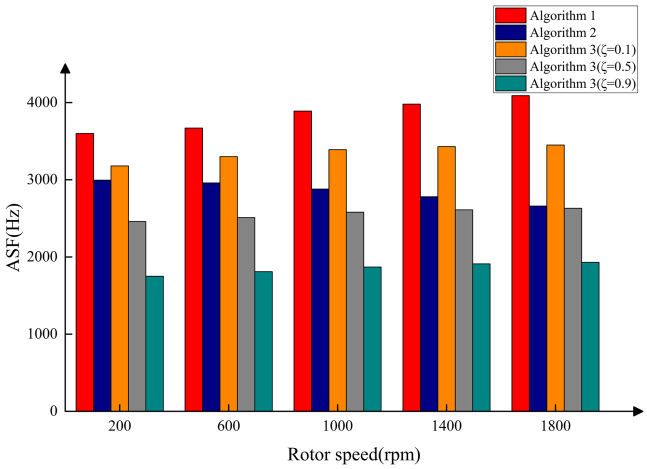

Fig. 15. Comparison of ASF under different operating conditions at the identical sampling frequency of 10 kHz.

other hand, regardless of the value of ζ, the ASF of Algorithm 3 remains relatively stable as the motor speed increases from 200 to 1800 r/min. This indicates that the dynamic threshold updating mechanism in Algorithm 3 effectively prevents the triggering condition from being overly sensitive to threshold errors caused by speed variations. In addition, when the adjustable coefficient ζ increases from 0.1 to 0.9, the ASF of Algorithm 3 decreases significantly, demonstrating the flexibility and effectiveness of the proposed method in reducing the switching frequency.

According to [27], switching loss is proportional to the switching frequency. Therefore, based on the switching frequency data at 1000 r/min, if the switching loss of Algorithm 3 with an adjustment coefficient $\zeta = 0.5$ is assumed to be 1 p.u., the relative switching loss ratios for Algorithm 1, Algorithm 2, Algorithm 3 ($\zeta = 0.1$), and Algorithm 3 ($\zeta = 0.9$) are approximately 1.38, 1.12, 1.26, and 0.72 p.u., respectively. It can be seen that the proposed ET-MPC method can significantly reduce the switching losses.

Under the identical sampling frequency of 10 kHz, the impact of parameter mismatch severity and adjustable coefficient on the ASF of the proposed Algorithm 3 was analyzed using MATLAB simulations, as presented in Fig. 16. The motor operated at a speed of 1000 r/min under rated load. The variation range of each parameter is set from 0.5 to 1.5 times its nominal value, with an interval of 0.1 times the nominal value. It can be observed that the ASF of the proposed Algorithm 3 decreases significantly as the adjustable coefficient increases. This is because a larger adjustable coefficient in the threshold condition results in a longer control update interval in the proposed ET-MPC scheme. In the entire range of parameter variations, the variation of ASF remains very stable without significant fluctuations, indicating the good robustness of the proposed dynamic threshold compensation-based ET mechanism.

D. Computational Burden Analysis

To verify the effectiveness of the proposed method in reducing the computational burden, the average execution times (AETs) of the three algorithms were measured using the real-time profiling tool provided by the dSPACE platform, as summarized

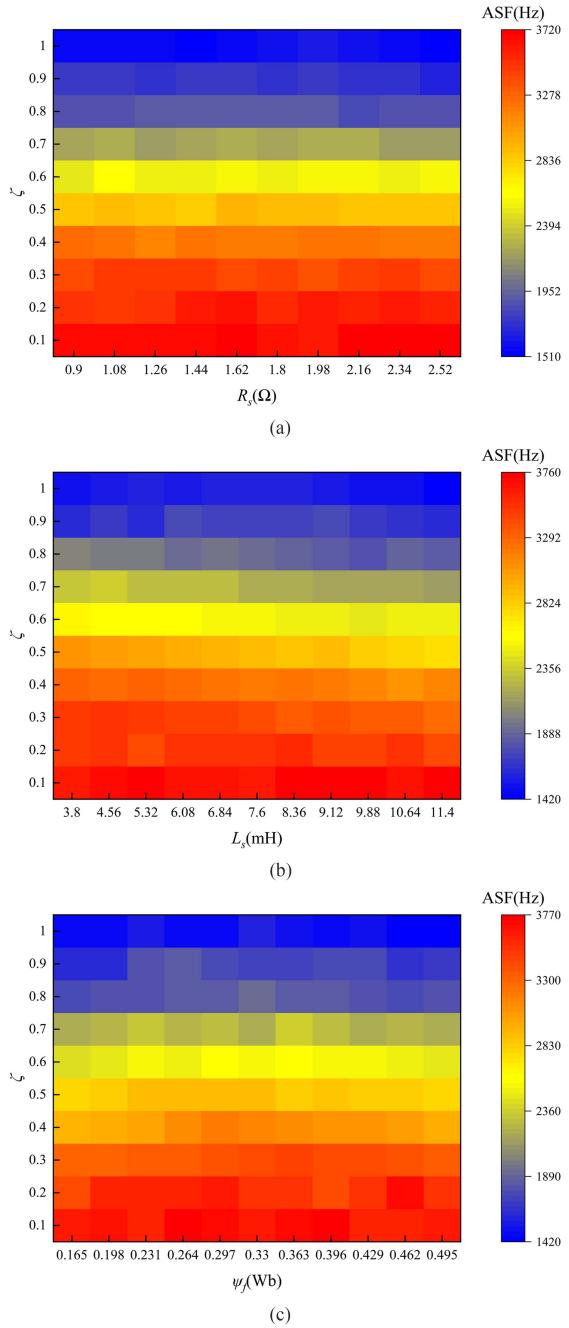

Fig. 16. Impact of parameter mismatch severity and adjustable coefficient ζ on the ASF of the proposed Algorithm 3 under the identical sampling frequency of 10 kHz. (a) Resistance R_s mismatch severity. (b) Inductance L_s mismatch severity. (c) Flux linkage ψ_f mismatch severity.

in Table III. Algorithm 1 exhibits the highest computational cost at 25.56 μs, as it performs complete prediction and optimization in every sampling cycle. Algorithm 2 reduces the AET to 22.53 μs by skipping redundant updates when the triggering condition is not met, thereby decreasing the frequency of full optimization steps. The proposed Algorithm 3 further improves computational efficiency through its dynamic threshold compensation mechanism. This mechanism allows the control strategy to adaptively adjust the update rate based on system deviation, thereby maintaining control accuracy while reducing

TABLE III
COMPUTATIONAL BURDEN COMPARISON OF THE THREE ALGORITHMS

	Algorithm 1	Algorithm 2	Algorithm 3	
AET (μs)	25.56	22.53	$\zeta = 0.1$	24.34
			$\zeta = 0.3$	23.36
			$\zeta = 0.5$	22.15
			$\zeta = 0.7$	20.97
			$\zeta = 0.9$	19.56

computational load. As the adjustment coefficient ζ increases from 0.1 to 0.9, the AET decreases from 24.34 to 19.56 μs. This trend indicates that higher ζ values correspond to less frequent triggering events, leading to fewer optimization calculations and lower AET.

V. CONCLUSION

To address the challenges of high switching frequency, this article introduces a dynamic threshold adjustment-based ET-MPC method for PMSM. In addition, an adjustable coefficient is employed to flexibly reduce the switching frequency. The key novelty lies in the dynamic adjustment of the threshold inequality in the ET technique. The experimental evaluations under similar switching frequency, identical sampling frequency, and both accurate and mismatched parameters confirm that the proposed strategy effectively reduces unnecessary switching actions, and maintains robust performance under system variations. Switching frequency and computational burden analyses further demonstrate its adaptability for practical implementation. Furthermore, the influence of selecting adjustable coefficients on the control system was further analyzed. It was demonstrated that adjustable coefficients enhance the flexibility.

REFERENCES

[1] P. Karamanakos and T. Geyer, "Guidelines for the design of finite control set model predictive controllers," *IEEE Trans. Power Electron.*, vol. 35, no. 7, pp. 7434–7450, Jul. 2020.

[2] B. Yu, W. Song, K. Yang, Y. Guo, and M. S. R. Saeed, "A computationally efficient finite control set model predictive control for multiphase PMSM drives," *IEEE Trans. Ind. Electron.*, vol. 69, no. 12, pp. 12066–12076, Dec. 2022.

[3] M. T. Zhao, S. Wu, and S. Cui, "Multiphase PMSM with asymmetric windings for more electric aircraft," *IEEE Trans. Transp. Electrif.*, vol. 6, no. 4, pp. 1592–1602, Dec. 2020.

[4] J. Z. Bird, "A review of electric aircraft drivetrain motor technology," *IEEE Trans. Magn.*, vol. 58, no. 2, Feb. 2022, Art. no. 8201108.

[5] M. Gu, Z. Wang, K. Yu, X. Wang, and M. Cheng, "Interleaved model predictive control for three-level neutral-point-clamped dual three-phase PMSM drives with low switching frequencies," *IEEE Trans. Power Electron.*, vol. 36, no. 10, pp. 11618–11630, Oct. 2021.

[6] A. Edpuganti and A. K. Rathore, "A survey of low switching frequency modulation techniques for medium-voltage multilevel converters," *IEEE Trans. Ind. Appl.*, vol. 51, no. 5, pp. 4212–4228, Sep./Oct. 2015.

[7] A. Edpuganti and A. K. Rathore, "Optimal pulsewidth modulation of medium-voltage modular multilevel converter," *IEEE Trans. Ind. Appl.*, vol. 52, no. 4, pp. 3435–3442, Jul./Aug. 2016.

[8] G. Chen, H. Peng, R. Zeng, Y. Hu, and K. Ni, "A fundamental frequency sorting algorithm for capacitor voltage balance of modular multilevel converter with low-frequency carrier phase shift modulation," *IEEE J. Emerg. Sel. Top. Power Electron.*, vol. 6, no. 3, pp. 1595–1604, Sep. 2018.

[9] T. Geyer and D. E. Quevedo, "Performance of multistep finite control set model predictive control for power electronics," *IEEE Trans. Power Electron.*, vol. 30, no. 3, pp. 1633–1644, Mar. 2015.

[10] Z. Zhang, J. Ma, L. Qiu, X. Liu, B. Xu, and Y. Fang, "Extended ISMO-based two-step prediction horizon model-free predictive control for power converters," *IEEE J. Emerg. Sel. Top. Power Electron.*, vol. 13, no. 1, pp. 408–417, Feb. 2025.

[11] C. Liu and J. Shang, "Three-dimension space vector based finite control set method for OW-PMSM with zero-sequence current suppression and switching frequency reduction," *IEEE Trans. Power Electron.*, vol. 36, no. 12, pp. 14074–14086, Dec. 2021.

[12] J. Böcker, B. Freudenberg, A. The, and S. Dieckerhoff, "Experimental comparison of model predictive control and cascaded control of the modular multilevel converter," *IEEE Trans. Power Electron.*, vol. 30, no. 1, pp. 422–430, Jan. 2015.

[13] Y. Sangsefidi, S. Ziaeinejad, and A. Mehrizi-Sani, "Low switching frequency-based predictive control of a grid-connected voltage-sourced converter," *IEEE Trans. Energy Convers.*, vol. 32, no. 2, pp. 686–697, Jun. 2017.

[14] M. Preindl, E. Schaltz, and P. Thogersen, "Switching frequency reduction using model predictive direct current control for high-power voltage source inverters," *IEEE Trans. Ind. Electron.*, vol. 58, no. 7, pp. 2826–2835, Jul. 2011.

[15] V. Spudić and T. Geyer, "Model predictive control based on optimized pulse patterns for modular multilevel converter STATCOM," *IEEE Trans. Ind. Appl.*, vol. 55, no. 6, pp. 6137–6149, Nov./Dec. 2019.

[16] M. Vasiladiotis, A. Christe, and T. Geyer, "Model predictive pulse pattern control for modular multilevel converters," *IEEE Trans. Ind. Electron.*, vol. 66, no. 3, pp. 2423–2431, Mar. 2019.

[17] S. Vazquez et al., "Model predictive control: A review of its applications in power electronics," *IEEE Ind. Electron. Mag.*, vol. 8, no. 1, pp. 16–31, Mar. 2014.

[18] Y. -K. Fu, G. -H. Yang, H. -J. Ma, H. Chen, and B. Zhu, "Event-triggered feedforward predictive control for dimension quality optimization in BIW assembly process," *IEEE Trans. Ind. Informat.*, vol. 18, no. 2, pp. 1083–1090, Feb. 2022.

[19] C. Liu, H. Li J.Gao, and D. Xu, "Aperiodic robustmodel predictive control for constrained continuous-time nonlinear systems: An event-triggered approach," *IEEE Trans. Cybern.*, vol. 48, no. 5, pp. 1397–1405, May 2018.

[20] D. Antunes and W. P. M. H. Heemels, "Rollout event-triggered control: Beyond periodic control performance," *IEEE Trans. Autom. Control.*, vol. 59, no. 12, pp. 3296–3311, Dec. 2014.

[21] M. Wang, J. Sun, and J. Chen, "Stabilization of perturbed continuous-time systems using event-triggered model predictive control," *IEEE Trans. Cybern.*, vol. 52, no. 5, pp. 4039–4051, May 2022.

[22] C. Liu, H. Li, Y. Shi, and D. Xu, "Codesign of event trigger and feedback policy in robust model predictive control," *IEEE Trans. Autom. Control.*, vol. 65, no. 1, pp. 302–309, Jan. 2020.

[23] H. Li and Y. Shi, "Event-triggered robust model predictive control of continuous-time nonlinear systems," *Automatica*, vol. 50, no. 5, pp. 1507–1513, 2014.

[24] Q. Sun, J. Chen, and Y. Shi, "Integral-type event-triggered model predictive control of nonlinear systems with additive disturbance," *IEEE Trans. Cybern.*, vol. 51, no. 12, pp. 5921–5929, Dec. 2021.

[25] B. Wang et al., "Event-triggered model predictive control for power converters," *IEEE Trans. Ind. Electron.*, vol. 68, no. 1, pp. 715–720, Jan. 2021.

[26] M. Zordan, P. Vas, M. Rashed, S. Bolognani, and M. Zigliotto, "Field-weakening in vector controlled and DTC PMSM drives, a comparative analysis," in *Proc. 8th Int. Conf. Power Electron. Variable Speed Drives*, 2000, pp. 493–449.

[27] A. Edpuganti and A. K. Rathore, "A survey of low switching frequency modulation techniques for medium-voltage multilevel converters," *IEEE Trans. Ind. Appl.*, vol. 51, no. 5, pp. 4212–4228, Sep./Oct. 2015.

Junqiang Luo was born in Hubei, China, in 2001. He received the B.S. degree in electrical engineering from Taiyuan University of Technology, Taiyuan, China, in 2023. He is currently working toward the M.S. degree in electrical engineering with the School of Electrical and Electronic Engineering, Huazhong University of Science and Technology, Wuhan, China.

His major research interests include permanent magnet synchronous motor drives and model predictive control.

Yixiao Luo (Member, IEEE) was born in Hubei, China, in 1991. He received the B.Eng. degree in electrical engineering from Wuhan University, Wuhan, China, in 2013, the M.Eng. degree in electrical engineering from Hanyang University, Seoul, South Korea, in 2015, and the Ph.D. degree in electrical engineering from the City University of Hong Kong, Hong Kong, in 2019.

Since March 2022, he has been an Associate Professor with the School of Electrical and Electronic Engineering, Huazhong University of Science and Technology, Wuhan. His research interests include permanent magnet motor drives, power electronics, renewable energy sources, and microgrids.

Kai Yang (Senior Member, IEEE) received the B.S., M.S., and Ph.D. degrees in electrical engineering from Huazhong University of Science and Technology (HUST), Wuhan, China, in 1998, 2000, and 2003, respectively.

In 2005, he was with the Department of Electrical Machine and Control Engineering, School of Electrical and Electronic Engineering, HUST. He is currently a Professor with the School of Electrical and Electronic Engineering, HUST. He is the Secretary General for ICEMS 2008, and the topic chair for ICEMS 2016/2017/2018/2019. He has authored and coauthored more than 100 technical papers on IEEE conferences and journals, and has 30 authorized Chinese patents. His research interests include functional-material actuators, design, and control of ac motors.

Dr. Yang has been the Fellow of IET since 2023. He is a Technical Reviewer for IEEE TRANSACTIONS ON POWER ELECTRONICS, IEEE TRANSACTIONS ON INDUSTRIAL ELECTRONICS, and IEEE TRANSACTIONS ON INDUSTRY APPLICATIONS.

Md Sazzit Hossen was born in Satkhira, Bangladesh. He received the B.E degree in electrical engineering and automation from Southwest Petroleum University, Chengdu, China, in 2023. He is currently working toward the M.S degree in electrical engineering with the School of Electrical and Electronic Engineering, Huazhong University of Science and Technology, Wuhan, China.

Jincheng Yu (Member, IEEE) received the B.E. degree in electrical engineering from the Beijing Jiaotong University, Beijing, China, in 2016, and the Ph.D. degree in electrical and electronic engineering from the School of Energy and Environment, City University of Hong Kong, Hong Kong, in 2020.

She is currently an Assistant Professor with the Department of Electrical Engineering, Harbin Institute of Technology, Shenzhen, China. Her research interests include machine design and control, and sustainable energy conversion technologies.